BERGISCHE
UNIVERSITÄT
WUPPERTAL

Analysis of data from lightning detector stations for the Pierre Auger Observatory

Bachelor Thesis

zur Erlangung des akademischen Grades
Bachelor of Science im Fach Physik

der Fakultät für Mathematik und Naturwissenschaften
der Bergischen Universität Wuppertal

vorgelegt von
Simon Strotmann

Wuppertal, 20. April 2016

Betreuender Professor:	Prof. Dr. Karl-Heinz Kampert
Zweitkorrektor:	Prof. Dr. Christian Zeitnitz

Contents

1 Introduction **3**

2 Cosmic Rays **4**
2.1 Flux and Origin 4
2.2 Primary particle composition 5
2.3 Extensive air shower 5

3 Lightning Physics **7**
3.1 Thunderstorm conditions 7
3.2 Classification of lightning discharges 7
3.3 Electrical Breakdown 10
3.4 Radio emission 11

4 The Pierre Auger Observatory **13**
4.1 Hybrid Detection: Surface and Fluorescence Detector 13
4.2 Additional developments and atmospheric surveillance 14

5 Lightning Detection with the Boltek StormTracker **16**
5.1 Properties of the Boltek StormTracker 16
5.2 StormTracker usage of CheckUp-System 17
5.3 Deployment of the StormTracker at the Pierre Auger Observatory and at the University of Wuppertal 17

6 Data Analysis of lightning radio events **18**
6.1 Data Acquisition 18
6.2 Development of the EventBrowser 19
6.3 Frequency spectrum of traces and examination of the band-pass 21
6.4 StormTracker data comparison with CheckUp-System data 25
6.5 Analysis for polarity determination 26
6.6 Brief analysis of multiplicity and pulse lengths 32

7 Conclusion **34**

A Comparison of the polarity from traces to Checkup file **35**

List of figures **39**

1. Introduction

Amongst many scientific phenomena yet unexplained, in this thesis we want to have a look at two of the most spectacular research fields in astroparticle and geo physics.

To begin with cosmic rays, there are still open questions since their first discovery by Victor F. Hess in 1912 respective their origin, their energy sources which accelerates them up to 10^{20} eV and their maximum energy. The Pierre Auger Observatory aims for disclosing the secrets of these mysterious high-energetic particles.

Another spectacular phenomenon in nature which, in contrast to cosmic rays, is visible to the human eye, are lightnings.
Although everybody may have seen one and many wondered about this high-voltage discharge, a final explanation about their ignition is yet missing.

Recent studies [1] suggest a correlation between detected events of cosmic rays at the Pierre Auger Observatory and the occurrence of lightning events measured via radio detection, which would be a fascinating interdisciplinary result of combining efforts of two different research fields.

One promising approach for the detection and characterization of lightnings is the measuring of electromagnetic bipolar pulses in the radio frequency range with the commercial StormTracker from Boltek.

To stage a fundament for the main data analysis of radio trace features, the first part of this thesis comprises an introduction to cosmic rays in Sec. 2 as they are the primordial effect, a summary of lightning physics as it is understood and a section about the runaway breakdown theory during extensive air showers in Sec. 3, and finally a brief introduction to the Pierre Auger Observatory and its facilities in Sec. 4
The emphasis of the radio detection of lightnings with the Boltek StormTracker is treated thereafter in Sec. 5

The center part is the data analysis of the radio traces detected with the StormTracker after determining the antennas sensitivity frequency range in Sec. 6 with a following conclusion in Sec. 7.

2. Cosmic Rays

The first discovery of Cosmic Rays was made by Viktor Hess 1912 carrying out several balloon flights equipped with a pressure-resistant electrometer at the atmosphere to prove the existence of cosmic radiation. This cornerstone being laid, the research field of astroparticle physics was established to study cosmic rays, their flux measured on the earth, their origin and their composition.
In this section we briefly want to summarize the results of the latest research.

2.1. Flux and Origin

Cosmic rays are charged particles traveling through the interstellar medium with nearly speed of light.
While cosmic rays with modest energy can be detected directly, e.g. with atmospheric balloons, high-energy cosmic rays are observed indirectly: As a charged particle hits the atmosphere of the earth at a height of about 20 km, a cascade of particles is created due to collisions with the atmosphere's matter. This cascade of different generations of secondary particles is called an extensive air shower (EAS), which can be seen in Fig. 3 and is described later in detail in Sec. 2.3.

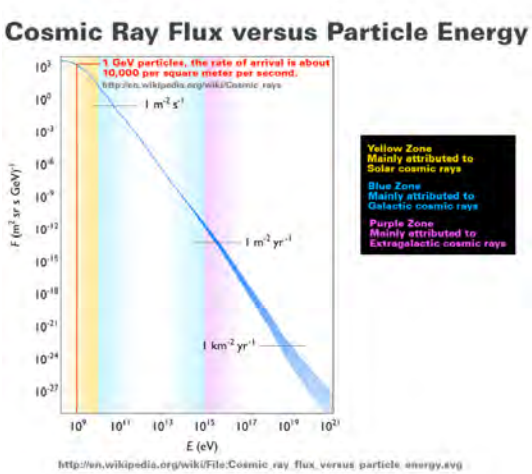

Figure 1: Cosmic Ray Flux with respect to the energy, showing three main regions, from [2]

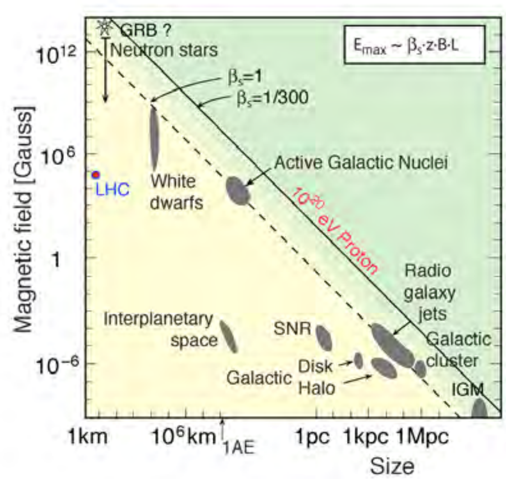

Figure 2: Hillas Plot showing magnetic field of possible sources with respect to the size, from [3]

On their way through the universe, some cosmic rays also reach the earth with a flux depending on their energy, according to a power law:

$$\frac{dE}{dN} \propto E^{-\gamma}, \qquad (1)$$

where γ is the spectral index, which occupies values between $\gamma \approx 2.6$ and $\gamma \approx 3.0$ according to the three main regions as seen in Fig. 1.
While we are strafed by tens of thousands of cosmic rays in the GeV region each second, the very low flux of cosmic rays with highest energies (e.g. 1 particle km^{-2} year^{-1} at about $E = 10^{19}$ eV) make huge areas like the surface detector (see Sec. 4) of the Pierre Auger Observatory necessary to achieve an adequate detection statistics.

As Fig. 1 suggests, the sources of cosmic rays in the low energy spectrum are attributed to solar activity, whereas moderate-energy cosmic rays and high-energy cosmic rays are attributed to galactic, respectively extragalactic sources.

Considering the sources and the acceleration process there are two approaches: The Bottom-Up and the Top-Down Model.
The Top-Down Model explains the creation of high energetic particles as a result of a decay of exotic super-massive particles with $E > 10^{20}$ eV as relicts from energy processes in the early state of the universe.

The Bottom-Up Model explains the high energy of cosmic rays with an acceleration from gigantic magnetic fields. Deduced from the Fermi acceleration and the Blanford and Ostriker mechanism we can take the following formula with respect to the Hillas Plot shown in Fig. 2 into account:

$$E_{\text{max}} \approx \frac{1}{2}\beta_{\text{s}}\frac{B}{\mu\text{G}}\frac{L}{\text{kpc}} \cdot Z \cdot 10^{18}\ \text{eV} \tag{2}$$

where E_{max} is the maximum energy the cosmic rays is able to gain from the acceleration process, β_{s} is the shock velocity of particles accelerated mainly by shocks of solar flares or supernova remnants, B the magnetic field strength in μG, L the size of magnetic field region in kpc and Z the atomic number.

Thus, taking a look to the Hillas plot, for the dashed line with $\beta = 1$ we can identify active galatic nuclei, radio galaxy jets or galactic clusters as possible sources for high-energetic cosmic rays.

2.2. Primary particle composition

Depending on the energy of the primary particle one can measure the primary particle composition directly or indirectly.
Due to the high flux of cosmic rays with $E < 1$ TeV (see [4] in comparison to Fig. 1) the primary particle composition can be determined to ~87% protons, ~12 % He-atoms, 2% electrons, 1% heavier nuclei such as C, O, Fe, γ - rays and neutrinos.

In general the isotope abundance is quite similar to the solar system one, but with differences respective to a lower amount of H and He atoms and a higher amount of light elements such as Li, Be and B (compare Fig. 4) [5].
The range between $2 < Z < 5$ filled by cosmic rays can be explained by reactions with the interstellar medium.

For high-energetic cosmic rays the flux decreases. Consequently the determination of the composition has to be done indirectly by measuring secondary particles created in an extensive air shower, which is explained in the following chapter.

2.3. Extensive air shower

When a high-energetic cosmic ray interacts with an atomic nucleus of the atmosphere, it causes the creation of a variety of different particles, known as extensive air shower (EAS). Due to collisions with oxygen and nitrogen, neutrons, protons and pions are created (see Fig. 3). Neutral pions decay into two photons while the charged ones decay in muons and neutrinos and thus in electrons and more neutrinos [2].

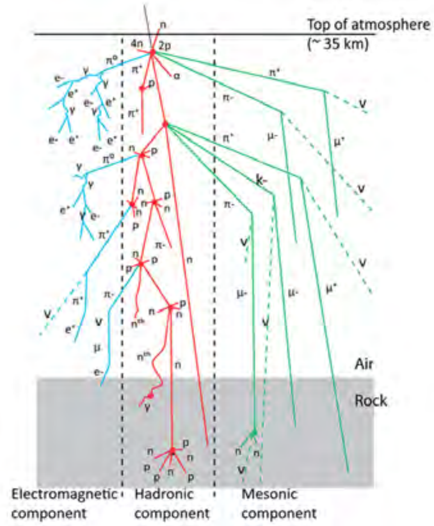

Figure 3: Schematic representation of an extensive air shower from cosmic rays, from [6]

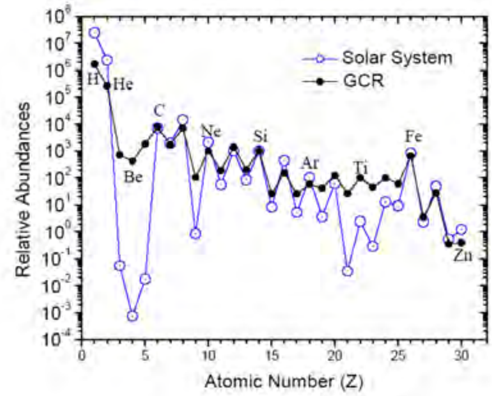

Figure 4: Relative abundances with respect to the atomic number Z from cosmic rays in comparison to the solar system , from [5]

$$\pi^0 \rightarrow \gamma + \gamma \qquad \pi^+ \rightarrow \mu^+ + \nu_\mu \qquad \pi^- \rightarrow \mu^- + \bar{\nu}_\mu$$

$$\mu^+ \rightarrow e^+ + \nu_e + \bar{\nu}_\mu \qquad \mu^- \rightarrow e^- + \nu_\mu + \bar{\nu}_e$$

Consequently, one can divide the shower into three components: an electromagnetic one, caused by the decay of the neutral pions into two photons with subsequent e^-e^+- pair production and electron bremsstrahlung; a muonic one and a hadronic one which consists mainly of pions and kaons [2].

Compton scattering, electron-positron pair production and ionization produce a significant amount of secondary electrons proportional to the energy of the primary cosmic ray. The average energy of the secondary electrons at ground is approximately 30 MeV [7].
Reaching the earth's surface, the geometry of an EAS is described as a "pancake-like structure" with thickness of a few meters and a certain width depending on the energy across the cosmic rays axis since the electromagnetic fraction of the cascade develops transversally due to the momentum-conserving decay of neutral pions [7].

3. Lightning Physics

Lightning is a common but violent phenomenon which triggered fear but also scientific curiosity form the beginning of human history.
Nevertheless the gaps in the theoretical understanding have not been able to be closed by current scientific research. In this section we will briefly discuss those parts that are thought to be understood reasonably well.

3.1. Thunderstorm conditions

One requirement for the evolution of lightning are thunderclouds, which consist of regions of different charge providing an electric field. Usually, such a cloud contains an area of positive charge on top with a negatively charged area of approximately equal size underneath. An additional small area of positive charge can be found on the very bottom of the cloud.

There are various mechanisms that can lead to this charge separation and hence the polarization of the cloud:

Firstly, water from the earth's surface evaporates, rises towards the cloud and condenses to drops of water once it reaches the cloud.
Here collisions between the upwards-driven moisture and cloud particles strip off the electrons and consequently yield to ionization.
Secondly, freezing temperatures play a key role in polarization: When the moisture encounters the low temperatures inside the cloud (well below zero degree), it gets frozen and clusters together.

The upwards directed movement of those small ice crystals leads to a collision with hail particles of frozen water drops already in the cloud. Since they are heavy, they undergo a downwards-directed movement or stay stationary in the updraft of the thunderstorm [8]. Encounter of those two once more yields to ionization: The positively charged ice crystals continue to move upwards whilst the negatively charged particles remain in the lower parts. This induced charge separation builds up the required electrical field.

The electrical field extends the size of the thunderclouds and polarizes ions on the ground by repelling electrons. Increasing polarization renders the electrical field surrounding the cloud stronger while the air serves as an insulator until the strong electrical field is capable of ionizing the air leading to a conductive plasma which leads to the requirement of lightning initiation.

3.2. Classification of lightning discharges

A typical thunderstorm takes about 40-60 minutes with one lightning flash occuring in 20-30 seconds, originating in an approximately circular cloud of 6 to 10 km in diameter. It is common to distinguish between two kinds of lightning flashes: flashes reaching the ground (cloud-to-ground lightning) and flashes which either develop within the cloud (intracloud lightning) or spread to the surrounding air (cloud-to-air lightning), compare Fig. 5. All types of lightning can be further distinguished by their sign of charge and propagation direction of the initial charge leader. About 90% are negative and 10% are positive charged cloud-to-ground lightning, whereas up-going lightnings are very rare and mostly human initiated [8].

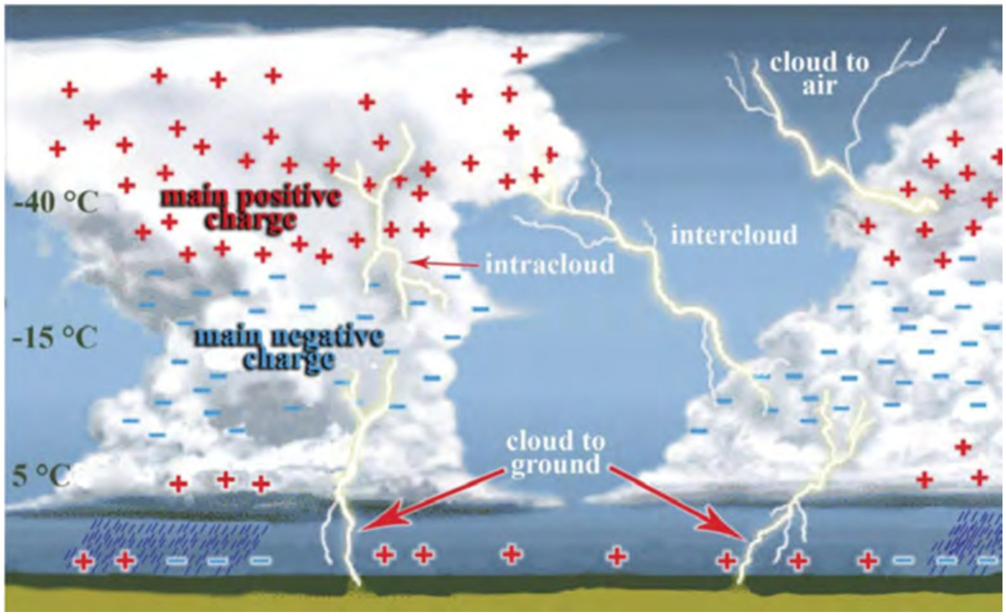

Figure 5: Scheme of different kind of lightnings: Intracloud, inter cloud, cloud-to-ground and charge regions within clouds, from [8].

The development of a lightning discharge is described using the case of cloud-to-ground downward lightning seen in Fig. 6 since this is the most frequent one.

In the beginning there is the occurence of a local discharge between the bottom of the main negative area and the small positive area underneath it, which causes the mobilization of electrons that have previously been fixed due to their attachment to the heavy particles [8]. As the electrons have very little mass (511 keV), they are extremely mobile and thus react significantly when exposed to an electrical field. Hail, ice, graupel and water remain almost stationary during the lightning.

Overrunning the small positive area, the electrons neutralize a significant fraction of that charge, before continuing traveling towards the ground through electric conductive channels of partially ionized gas, called 'stepped leaders'.
Due to inhomogeneous conductivity in certain regions between the cloud and the ground (most probably because of dust particles), the lightning bolt moves along discrete luminous segments often separated in different branches with tens of meter within a time interval from $\sim$50μs to $\sim$10μs while getting closer to the earth's surface.
On average, it takes 20 ms for a stepped leader to build up between the cloud and the ground with an average current of $<I> = 100$-200A.

The first return stroke and consequently the primary lightning current path is initiated after the attachment process of the downward going lightning branches and the positive charge build-up on the conducting earth's surface after the rendered electrical field exceeded a certain value.
Due to the high current of $\sim$30 kA, the region of the channel heats up rapidly to temperatures of 30.000 °C and causing an expansion of the air producing the shockwave thunder [8].

At this point, one has to distinguish between two scenarios: the one of the single-stroke flash when the current ceases to flow after the stroke and no new discharge is going to

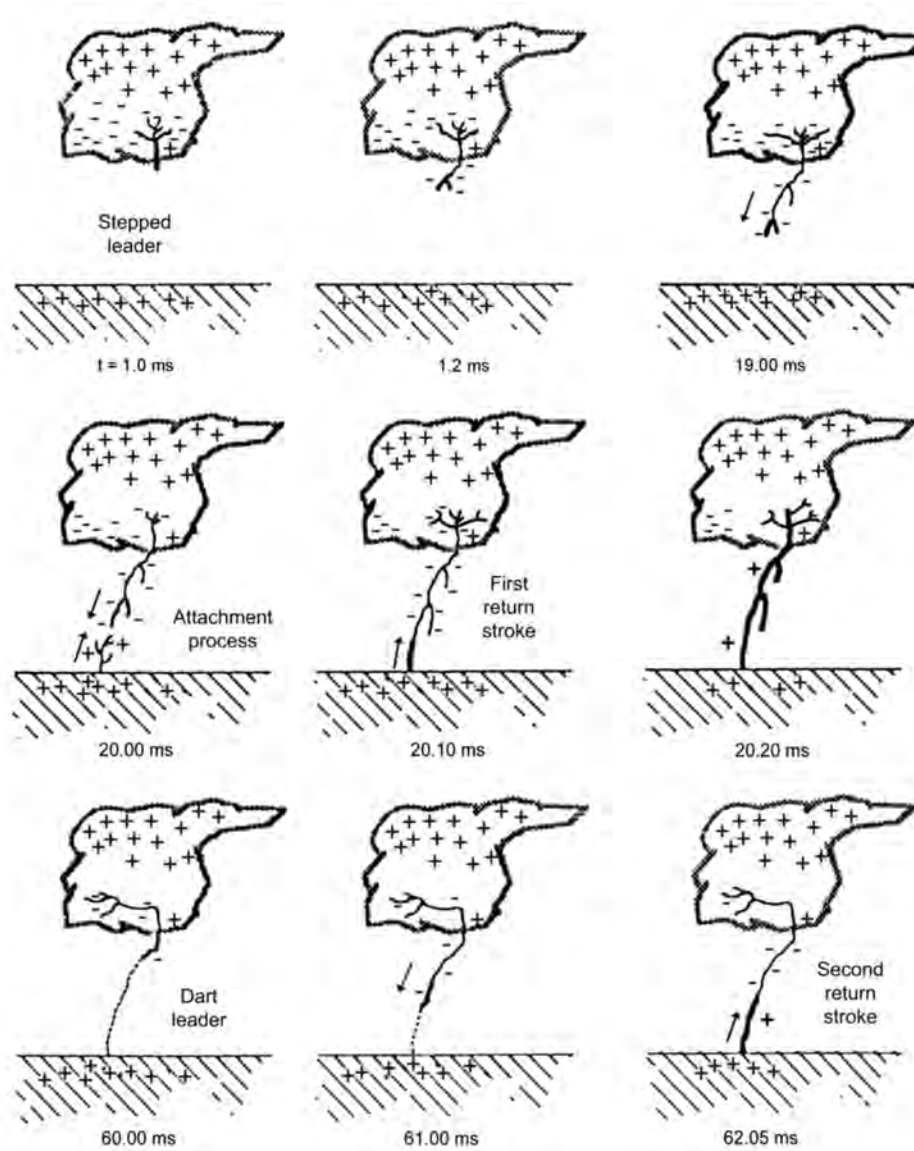

Figure 6: Schematic representation of the negative cloud-to-ground lightning discharge process, from [8].

follow. In this case, the lightning ends here; whereas in the multi-stroke flash scenario (which happens at about 80% of the cases), the first return stroke is followed by three to five smaller strokes, separated by 40-50ms.

In the second scenario, subsequent strokes are only generated if additional negative charge is replenished by the upper part of the previous stroke channel in a time less than about 100ms after the extinction of the previous current. The subsequent leaders, called 'dart leaders', follow the stepped leader's path and carries about 10% of the stepped leader's charge and a decreased current of half to a third of the first one's. With the dart leaders only following the main path, the subsequent return strokes are significantly less branched than the first one [8].

3.3. Electrical Breakdown

Lightning initiation requires the thunderstorm conditions presented in the Sec. 3.1, but the sheer existence of an corresponding electrical field is not sufficient for the discharge of lightning. This is why one has to consider the concept of the electrical breakdown.

In general, the conventional breakdown is a self-sustaining discharge producing a rapid increase in atmospheric conductivity leading to a collapse of the electrical field [8]. Considering the tail of the thermal distribution of electrons at about 10-20 eV fast electrons ionize matter generating new free electrons.
If the electric field exceeds a certain threshold $E > E_{\mathrm{thr}}$ the ionization-induced generation rate surmounts the recombination rate leading to an exponential increase of electrons. Taking the mean electron energy of several eVs during ionization into account the critical electric field can be determined to $E_{\mathrm{thr}} \approx 2\frac{\mathrm{MeV}}{\mathrm{m}}$ as the field strength scales linearly with air density [7]. Actual measurements (compare Fig. 7) in thunderclouds show a significant deviation from the electric field of about one order of magnitude E_{thr}. Thus, there is an urge of a mechanism sufficiently explaining the lower threshold required for lightning initiation.

One concept is known as runaway breakdown and is based on effects and properties of interaction of fast particles with matter.
Based on the Bethe-Heitler equation [9], electrons are under the influence of a braking force F due to ionization losses decreasing inversely proportional to their energy ϵ, as shown in Fig. 8.

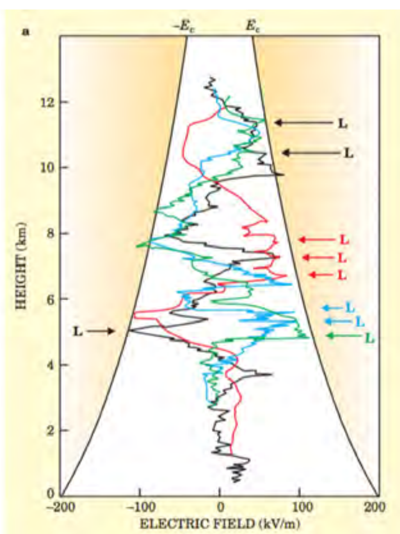

Figure 7: Results of measurements [10] of the electric field including zones of lowered threshold due to runaway breakdown with respect to the atmospheric height, from [7].

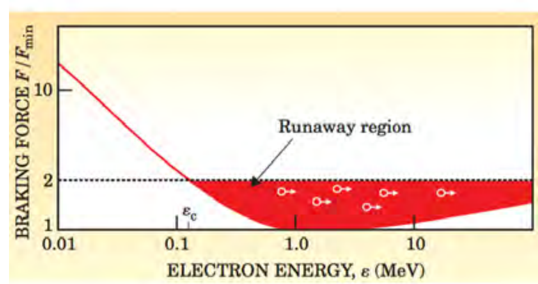

Figure 8: Braking force F/F_{min} with respect to the electron energy in MeV: Runaway region for $\epsilon > \epsilon_c$, from [7].

The reason for this circumstance lies in Coulomb's law.
It states that the interaction of fast electrons with fellow electrons or neutral nuclei treats the latter two as free particles. If in Coulomb scattering one combines the inverse squared proportionality of the Rutherford cross section σ to the electron energy ϵ with the dependency of the braking force F on the electron energy, the cross section and the molecular

density N_m, one ends up with a single inverse proportionality of the braking force to the electron energy:

$$\sigma \sim \epsilon^{-2} \qquad F \sim \epsilon\sigma N_m \qquad \longrightarrow F \sim \epsilon^{-1}.$$

With rising electron energy, the braking force F_{min} decreases until relativistic effects start and starts to grow again [7].
With the frictional scattering probability dropping, the acceleration of electrons gains relevance: A constant electrical field bigger than a critical value $E_{\text{crit}} = F_{\text{min}}/e$ yields continuous acceleration of electrons with $\epsilon > \epsilon_{\text{crit}}$.
Those electrons are called *runaway electrons*.

Instead of slowing down because of ionization losses, the runaway electrons obtain energy $\epsilon \approx mc^2 E_c/2E$ from acceleration in the electric field. Due to collisions with gas molecules, they create a large amount of slow thermal electrons and additionally new fast electrons with $\epsilon > \epsilon_{\text{crit}}$ which under the action of the field E_{crit} become runaway electrons themselves. The large amount of thermal electrons ultimately leads to the formation of plasma, thus completing the formation of a runaway breakdown. [1].

The conventional breakdown threshold $E_{\text{conv, thr}} \approx 2\frac{\text{MeV}}{\text{m}}$ is then lowered by one order of magnitude to $E_{\text{crit}} \approx 200\frac{\text{keV}}{\text{m}}$ assuming the concept of runaway breakdown, compare Fig. 7.
The electrical field cannot reach values significantly higher than E_{crit}, but keeps approximately this value for a significant part of the thunderstorm's lifetime [1]. The complete theory of runaway breakdown can be found in [11].

As described in section 2.3 the EAS of a cosmic rays fulfills the requirements of such fast seed electrons for a runaway breakdown EAS discharge.
The ionization then makes lightning initiation possible due to a highly local conductive plasma [1].

3.4. Radio emission

In general, lightning emits a broadband of radio frequencies [12] especially in the kHz and MHz region (compare spectrum at Fig. 9 and [13]). The signal in the kHz region can be heard in an AM radio during lighting.
Induced by the electrical field during lightning initiation, the discharge creates a strong unipolar electric current pulse that leads to the generation of a bipolar radio pulse which is measurable from large distances.
The derivative of the current has one sign at the start point of the current and the opposite sign at the end point. Thus, the polarity of the radiation pulse depends on the derivative of the current [8].
This can be seen on Fig. 10.

Additionally, according to theory [1], a narrow bipolar radio pulse of a few MHz and a length of an order of μs is created by the runaway breakdown EAS discharge.
Experiments in Russia and Kazakhstan [7] and at LOPES [12] have shown that at the initiation of lightning, one can always detect an isolated bipolar radio pulse for intracloud lightning.

Because of the strict bandpass, it is not expected to measure this with the Boltek StormTracker, which is examined in chapter 6.

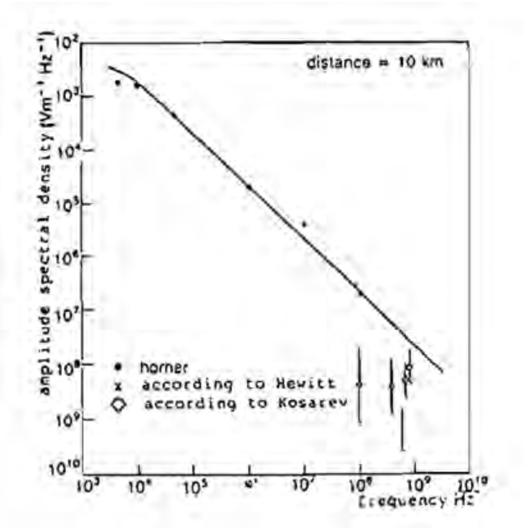

Figure 9: Radio emission spectrum from lightning, determined from a distance of 10 km, from [14].

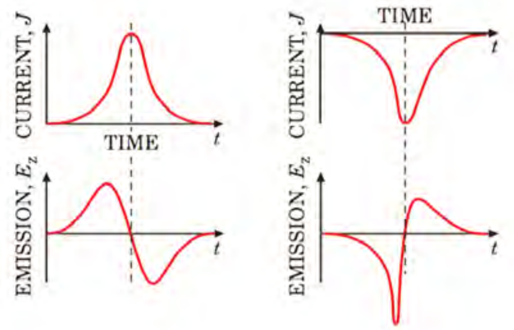

Figure 10: Theoretical predictions for radio pulse forms, modified from [7].

Nevertheless, radio signals are an important indicator for the question whether runaway breakdown EAS triggers lightning initiation.
One solution for correlation studies of cosmic ray and lightning would be to lower the measurement threshold of cosmic rays primaries at an energy of $\approx 10^{16}$ eV with a sufficient flux (compare Fig. 1) according to recent analysis of lightning statistics [15]. As described in the following chapter five Boltek StormTrackers are deployed at the Pierre Auger Observatory which detect lightning via radio emission.

Instead of lowering the detection threshold, the recorded data provided by the StormTrackers could also contain hints of lightning features and promise a cheap and independent detection method of radio signals or at least flag a lightning event for further analysis.

4. The Pierre Auger Observatory

The Pierre Auger Observatory is the largest detector for the investigation of high energy cosmic rays and the largest surface detector in general with a total area of more than 3000 km^2 located on a vast plain called the *Pampa Amarilla*.
Suggested by Jim W. Cronin and Alan A. Watson in 1992 and with the beginning of construction in 2000, its main goal is to investigate the origin, energy and composition of high-energy cosmic rays above 10^{18} eV.
In this section, a brief overview is given in order to present the frame of the research facilities in which the StormTracker is deployed.

4.1. Hybrid Detection: Surface and Fluorescence Detector

The complementary hybrid design in which ultrahigh energy cosmic rays are detected simultaneously, consists of the surface detector (SD) and the fluorescence detector (FD) delivering a high data reliability due to cross-check and measurement redundancy [16].

While the 1660 SD tanks measure the footprint of the EAS on ground level, the 24 FD telescopes are able to image the longitudinal development of the EAS cascade. Fig. 11 shows a map of the arrangement of the 1660 SD tanks surrounded by the four FD sites in Coihueco, Loma Amarilla, Los Leones, Los Morados.

A **surface detector** with a diameter of 3.6 m contains 12.000 l of ultra-pure water. With the help of three photomultiplier tubes symmetrically distributed on the surface, looking downward they detect Cherenkov light as charged relativistic particles traverse through the water. The SD station is powered autonomously with an average of 10 W by a solar power system [16]. Fig. 12 shows the tank with the important components.
Because of its independence of weather and time, the SD array provides a duty cycle of 100%.

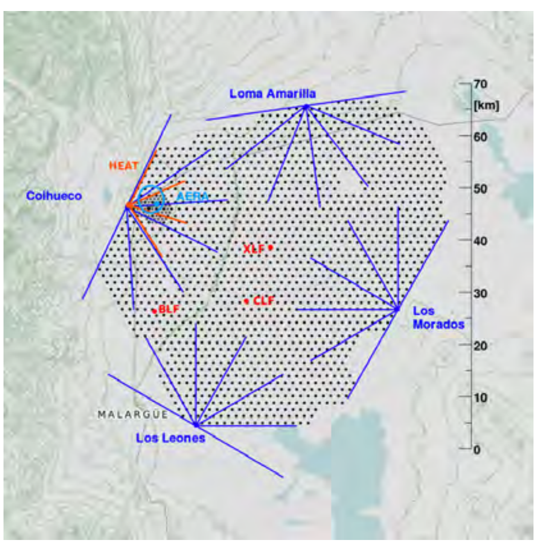

Figure 11: Map of the Pierre Auger Observatory, each black dot represents a SD tank. The whole area is surrounded by four FD sites, each equipped with 6 telescopes, from [17].

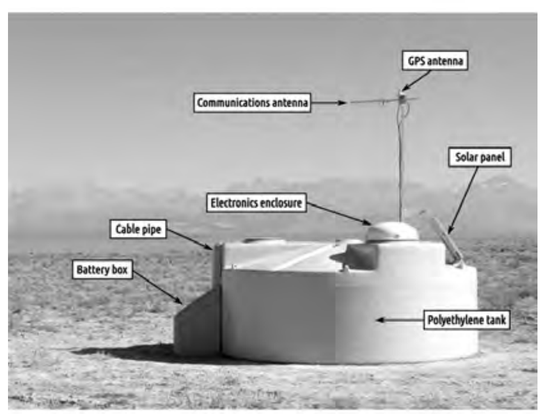

Figure 12: SD tank with labels of main components, from [16].

At each of the four sites marked in Fig. 11, six independent **fluorescence telescopes** are deployed. A single telescope has a field of view of 30° x 30° in azimuth and elevation with a minimum of 1.5° in elevation. Thus, the total coverage of the array viewed from every FD site at its perimeter sums up to 180° [16].
With the need of dark moonless nights, the duty cycle is up to $\sim$15%.
When particles collide in the atmosphere, they produce fluorescence light proportional to the energy deposit. So this observation method yields a calometric measurement of the cosmic ray's energy [16]. From the longitudinal profile of the energy deposit, the important observable $X_{\max}$, representing the atmospheric depth at which the shower reaches its maximum, can be determined.

In summary, the requirement of the hybrid design is to measure with at least one FD telescope the longitudinal development profile of cosmic rays above $E > 10^{19}$ eV during on-time cycle with "timing synchronization for simultaneous measurements of shower with the surface detector array" [16] .

4.2. Additional developments and atmospheric surveillance

Besides the SD array and 24 FD telescopes further facilities are built at the site of the observatory, which are briefly presented in this section.

On Fig. 11 one can see the infill area close to Coihueco representing additional 61 surface detectors paired with underground muon counters making up the **AMIGA** (Auger Muon and Infilled Ground Array) experiment.
It was designed to extend the range of sensitivity in cosmic ray detection down to $\sim 10^{17}$ eV and to measure only the muon component of the air shower in 2.5m underground. It also provides data to study the transition between extragalactic cosmic rays to galactic cosmic rays within this energy range.
Referring to Fig. 1 the flux increases rapidly with lower cosmic rays energy, thus - compared to the SD area - the smaller infill area of about 23,5 km^2 is sufficient for appropriate statistics. Because of the dense spacing of 750m, the infill detectors provides a low detection threshold and a high resolution.

In addition to AMIGA and on the basis of the well-proven concept of hybrid detection of FDs and SDs, three additional FD telescopes were built in front of the FD site at Coihueco - called **HEAT** (High Elevation Auger Telescope). They have the capability of a zenithal tilt of 29° extending the field of view over the before described AMIGA infill area up to 58° [16].

Another detection method of cosmic rays air showers is performed by the **AERA** (Auger Engineering Array).
Because air showers produce radio emission due to a geomagnetic and charge-excess mechanism (described in detail at [18]) it is detectable via radio antennas with a 100% duty cycle. The measured data in the VHF radio range promises to yield the determination of the primary cosmic rays energy, arrival direction and mass.
To study in which ways radio detection outperforms the cosmic rays detection mechanisms with SD and FD, the Pierre Auger Observatory collaboration is testing different prototypes taking advantage of the existing infrastructure of the observatory's hard- and software [16].
Further information for AMIGA, HEAT and AERA is provided by [19], [20] and [21].

The measurements from the facilities at the Pierre Auger Observatory highly depend on

the atmospheric conditions, which makes atmospheric surveillance obligatory.
Table 13 shows a summary of the important variables, their measurement devices and the frequency in which the results are obtained and Fig. 14 depicts their locations.

Category	Variable	Frequency	Instrument(s)
State	At ground: Pressure, Temp., Wind, Humidity	5 min	Weather Stations
	Profile: Pressure, Temp., Humidity	3 hours	GDAS[a]
Aerosols	Vert. Optical Depth (z)	hourly	CLF, XLF + FD
	Phase Function	hourly	2 APF units
	Ångström Coefficent	hourly	FRAM (HAM)
Clouds	Presence in FD pixels	15 min	4 Cloud Cameras
	Behind FD sites	15 min	4 lidar stations
	Along select tracks	avg. 1/night	FRAM, lidar
	Above CLF/XLF	hourly	CLF, XLF + FD

Figure 13: Summary of atmospheric conditions variables, from [16]

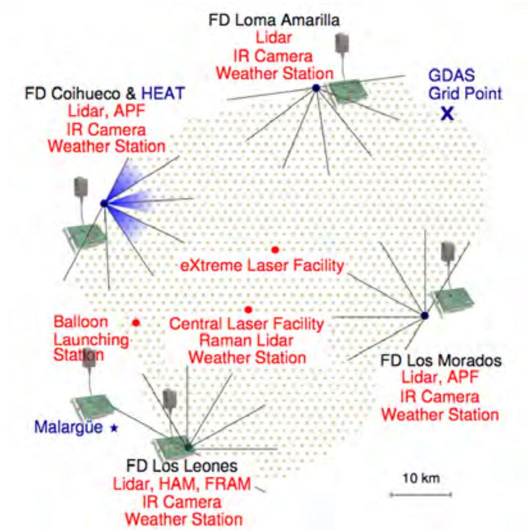

Figure 14: Locations of atmospheric monitoring devices, modified from [16]

In the context of this thesis, the surveillance of thunderstorm conditions and the detection of lightnings are the most important ones. The electrical field is observed at ground level with the help of two field mills, located at the AERA field obtaining data each second. The conditions for thunderstorms and lightnings are defined as following [22]:

$$\Delta_{\vec{E}} = |\vec{E}_i - \vec{E}_{i-1}| \qquad \Delta_{\vec{E}} > 2 \cdot \mathrm{RMS}_{1\mathrm{min}} \Rightarrow \text{thunderstorm condition}$$
$$\Delta_{\vec{E}} > 15 \cdot \mathrm{RMS}_{1\mathrm{min}} \Rightarrow \text{lightning discharge}$$

where $\vec{E}$ is the electric field which changes rapidly during thunderstorm conditions and $\mathrm{RMS}_{1\mathrm{min}}$ is defined as the RMS in the minute before the estimation is made.

Beside the lightning and thunderstorm detection with the $\vec{E}$-field mill, five *Boltek Storm-Trackers*, based on radio detection, are deployed at the observatory.
In the next chapter the deployment at the Pierre Auger Observatory and at the University of Wuppertal and their characteristics are presented.

5. Lightning Detection with the Boltek StormTracker

Before the deployment of the StormTracker stations at the Pierre Auger Observatory, they have been operated at the University of Wuppertal. Here, data from the commercial CheckUp System is available. Therefore, the data analysis has been developed with this data, but can be applied to the data of the Pierre Auger Observatory in the same way. The commercial product StormTracker from Boltek provides an easy deployment and enables an adequate and cheap data acquisition. In this chapter its properties and data management are described in detail.

5.1. Properties of the Boltek StormTracker

Consisting of an external PCI card used in a low-power consumption computer (Intel D2700MUD) and an external antenna connected with an ethernet cable, the Boltek StormTracker detects lightnings via radio detection within a radius of 1000 km.

Figure 15: Boltek StormTracker: PCI card with ethernet-connected antenna

The direction-finding radio antenna is sensitive within a frequency range of about $10 - 90$ kHz [22], whereas signal below or above this range is cut off as noise.
In later analysis this spectrum will be verified with the performance of Fourier transform..

The condition for recording an event is a sudden change in the electric field, which is mostly the case due to a discharge during lightnings inducing a bipolar radio pulse (see section 3.4). Based on the amplitude of the signal, the approximate distance is calculated.

Because Boltek provides almost no information about their products, most of the properties had to be determined in an experimental approach.
With a sampling rate measurement [22], using a function generator and a 13m long cable as an antenna, the sampling rate could be determined by fitting the detected trace with the known frequency of the sine generator.
The StormTracker has a sampling rate of 8 MHz resulting from the 125 ns per time bin

measurement. With a buffersize of 512 samples per event, we can observe traces within a timeframe of 64 μs.

5.2. StormTracker usage of CheckUp-System

CheckUp-System is a German company providing lighting event data, also detected with the Boltek Stormtracker, which grants data compatibility. Usually this data is sold to insurances as reference for reported damages due to lighting strikes.
For the lightning studies in this thesis, the data is useful in two manners:

Firstly to distinguish trusted lightnings events from undesired noise. Unfortunately, lightning radio emission does not represent the only source for radio signals in the observed frequency band.
At the test detection site at the University of Wuppertal, where the three StormTrackers were deployed as well as at the FD site locations in the Pampa Amarilla, we have to consider radio emission noise due to monitors, fluorescent tubes which emit a radio pulse when switched on and off, electric motors and many other possible sources.

Besides the exact time in μs, the north-south/east-west traces, distance, direction and the electric field, CheckUp-System determines also the polarity and estimates the field strength in three categories, moderate, strong and very strong.
So secondly, the provided data is useful for a comparison of extracted trace features.

5.3. Deployment of the StormTracker at the Pierre Auger Observatory and at the University of Wuppertal

Five Boltek StormTrackers are distributed at the FD sites in Coihueco, Loma Amarilla, Los Leones, Los Morados and Malargue at the campus site. This geometry allows an appropriate detection efficiency and allows easy maintenance being close to the FD sites and the campus (compare the half-transparent images of the StormTracker in Fig. 14)

It was shown [22] that the lightning detection system at the Pierre Auger Observatory fulfills the accuracy requirements respective to the reconstructed position (via time-of-arrival method).
The reconstructed position and the exact timestamp from the attached LEA-6T GPS extension module integrates in the Pierre Auger Observatory monitoring, as can be examined in Fig. 16 from http://mon.auger.uni-wuppertal.de.
At the BUW three StormTrackers were distributed within a radius of $\sim$ 10m (at latitude = 51.2456 and longitude = 7.1492) for the purpose of device comparability and an adequate statistic.
The deployment of three StormTrackers at the University of Wuppertal with the antennas pointing towards north was performed according to the instruction manual of the manufacturer [23].

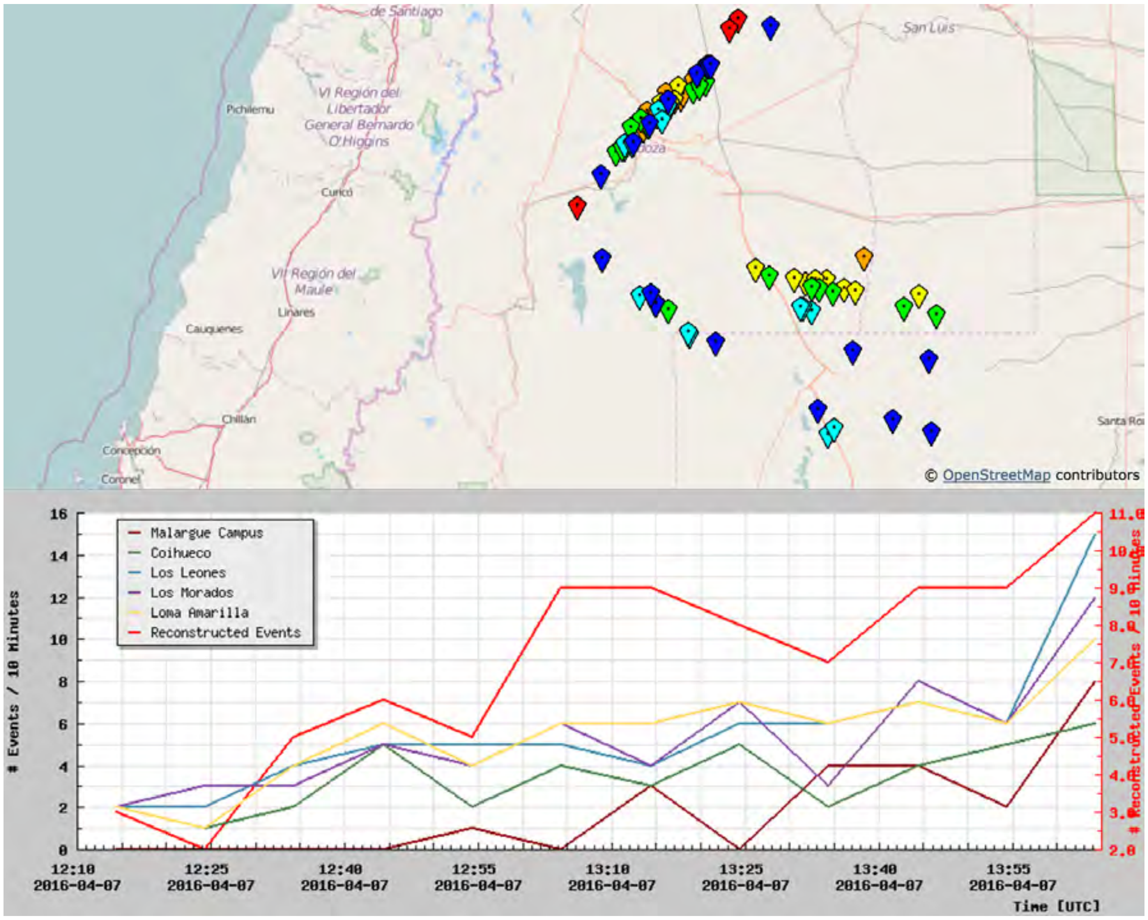

Figure 16: Monitoring of lightning events at the PAO, retrieved on 07.04.2016.

6. Data Analysis of lightning radio events

For the three detectors at the test site in Wuppertal a text file generated from the software of Boltek is the base of the analysis. Saved within this file are all events from each lightning detector measured within a selected timeframe. Details about the information that comes with the detection of each event is described in detail in Sec. 6.1. Just from the raw text file, it is not possible to have a look at the traces themselves, which made the development of an EventBrowser necessary and very useful.

Thus, in Sec. 6.2, the development of the EventBrowser for displaying the lightning radio traces is presented to give an insight of what is measured in general. Afterwards the sensitivity of the antennas is examined. It also examined, whether the measured frequencies of the traces are a result of the band-pass or the radio emission of the lightning discharge. At last, different possibilities to extract the polarity are studied and compared with the data from CheckUp System, which also contains an estimation of the polarity.

6.1. Data Acquisition

The recorded data can be readout in a raw/unreconstructed format which allows further studies. The interval of data acquisition was between the 1st of November 2012 at 00:00:59 when the first event recorded occurred and the 2nd of November 2012 at 09:09:27 when the last event was recorded.

In this data period, detector one triggered 1683 times, detector two 2468 times and detector three 1737 times.
As introduced above, the result of each of StormTracker is stored in a *.txt file. They contain the date and time with a precision of μs, the distance and direction in degrees of the detected lightning event, as well as the 512 values for the north/south and east/west antenna. These text files are converted into a root file for a more efficient data analysis.
The analysis of the files has also shown that for each of the 512 entries within one event, a value of 0 or 1 is stored, most probably representing a significant change in the electrical field value.

6.2. Development of the EventBrowser

There are three main reasons which made the development of an EventBrowser application useful within this thesis:

Firstly, opening the root files in the generic TBrowser in root is intricate, so all events detected by the selected detector are displayed in a list, ordered by time. For each detector and event the exact time, the direction (converted from radians to degrees) and the distance is displayed as the title of the histogram.
Secondly, to show time correlated lighting traces for direct comparison to crosscheck, if all detectors measured similar traces.
Thirdly, a comfortable tool was needed to directly compare the north-south and east-west traces and the electric field value, described above.

In Fig. 17, snapshots of the EventBrowser show one, two and three random events for a reasonable $\Delta t = 0$s, as this was visibly proven by comparing the traces for each detector of the same event within this timeframe. The distance d between each detector i and j in Wuppertal at the test site, as well as at the Pampa Amarilla, clearly undermatches the distance that radio waves propagate within Δt: $d_{i,j} \ll c \cdot \Delta t$.

The data of the root files are loaded within the `ReadFile()` function. It reads out the root file's trees and stores them into vectors `North`, `East` and `EField`, each containing the values within the buffersize of 512 bins.
Additionally, the vectors `Direction`, `Distance` and `UnixTime` are saved for each detectors separately.

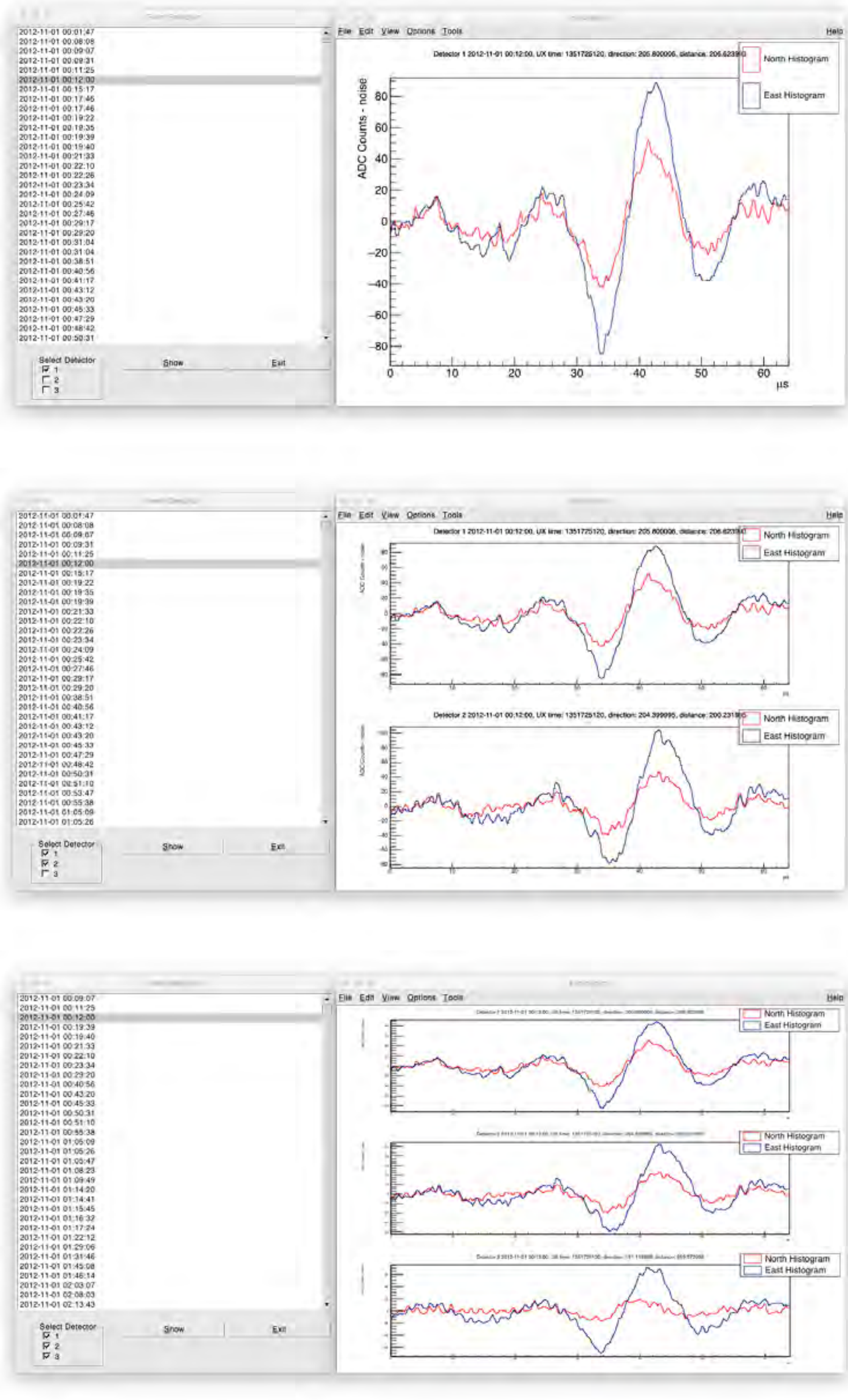

Figure 17: Snapshot of the EventBrowser for a randomly selected event with one (top), two (middle) and there (bottom) coincident stations. The list on the left side contains, depending on the selection of the three detectors, the intersection of coincident events and can be drawn to the right canvas.

In the title, all the information about the event is displayed. The direction is calculated on the base of the fraction of the two directions N/S and E/W, the distance depends on the amplitude. The quality of the data with respect to the accuracy of timing, direction and distance was already examined in [22].

For each detector a CheckBox is inserted into the root GUI. Depending on which CheckBoxes are checked, an intersection of coincidental events with $\Delta t = 0$ is generated. This is done by calling a function `in_both(vector a, vector b)` which selects in dependence on the entry of `UnixTime`, events that match the mentioned coincidence criterion. The list on the left side contains, depending on the selection of the three detectors, the intersection of coincident events. After selecting an event, one can draw the event to the right canvas.

Furthermore, the electrical field value can be mapped in color over the canvas to check a link to the behaviour of the traces. The background color blue is set for the value $E_{\text{thr}} = 0$ and yellow is set for $E_{\text{thr}} = 1$.
Because the direction-finding antennas solely measure the N/S and E/W traces, one can assume that if the slope of a trace exceeds a certain threshold value, $E_{\text{thr}} = 1$ is set to mark radio pulses.

Furthermore, after checking plenty of traces, it was obvious that $E_{\text{thr}} = 1$ is set, when the slope of the east trace increases rapidly. This is presented in Fig. 18 showing a typical trace for a detected lightning.

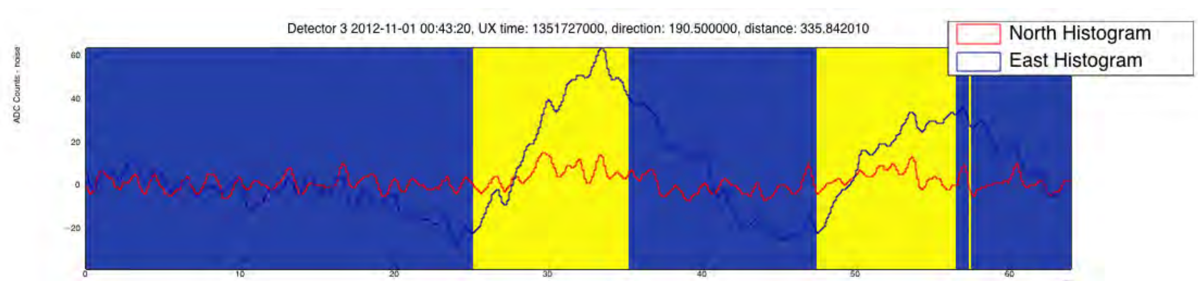

Figure 18: Example N/S and E/W trace for a defined lighting event with marked E_{thr} value, yellow for $E_{\text{thr}} = 1$, blue for $E_{\text{thr}} = 0$

.

In contrast to this, the north trace's slope seems not affect the corresponding E_{thr} value. The estimation of this value is made by internal code of Boltek.

In summary, the development of the EventBrowser facilitates the easy graphical analysis of selected lightning events. During the data analysis it was a very helpful, even necessary tool to have a quick look at trace features. It is made available in the svn repository at http://at-web.physik.uni-wuppertal.de/svn/LightningViewer.

6.3. Frequency spectrum of traces and examination of the band-pass

It is already known [22], that both antennas have a limited spectral sensitivity. In this section the influence of the antenna characteristics on the measured traces is examined. In order to determine the sensitivity of the antennas in the StormTracker, the individual traces were Fourier transformed and then compared to a filtered sharp pulse.

Fig. 19 demonstrates how this is performed for a typical radio event detected with one of the three detectors.

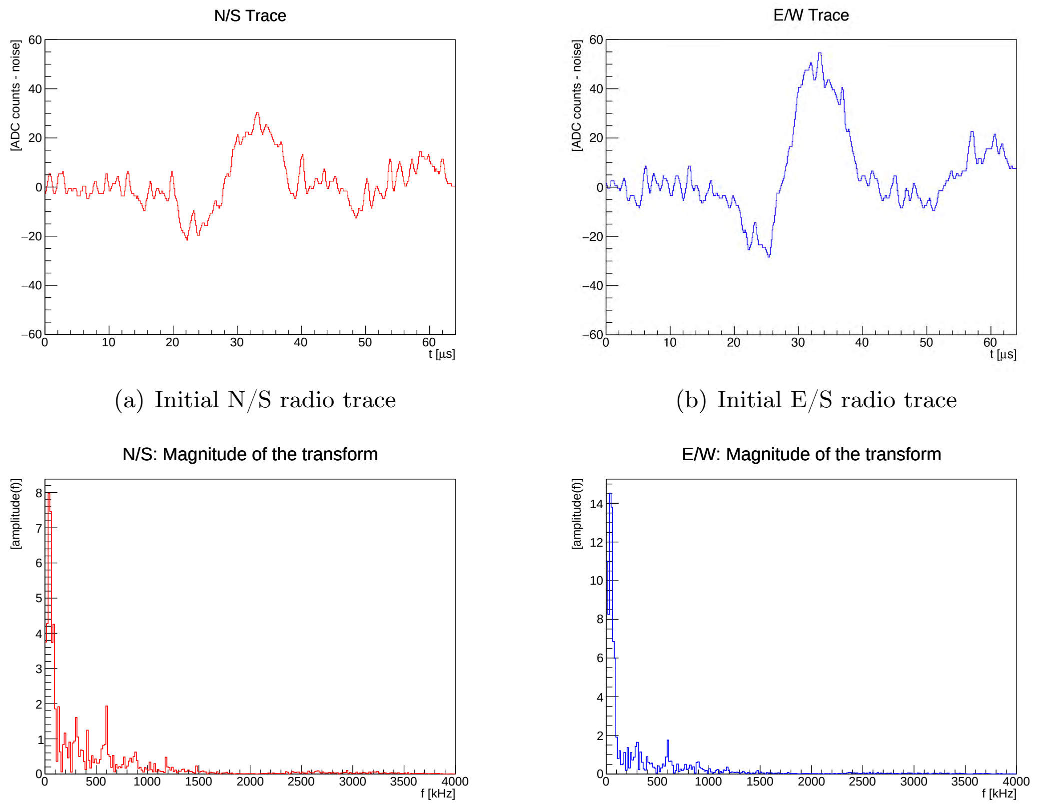

(a) Initial N/S radio trace

(b) Initial E/S radio trace

(c) Fourier transform of N/S radio trace

(d) Fourier transform of E/W radio trace

Figure 19: Initial traces for east/west and north/south orientation

According to the Nyqvist-Shannon sampling theorem, the $f_{\text{nyquist}} = \frac{1}{2} \cdot f_{\text{samplerate}}$ total frequency bandwidth is half the sampling rate of a discrete signal processing system, which is in this case $f_{\text{nyquist}} = 4000$ kHz.

Referring to [22], the sensitivity of the antenna is assumed to be between 10 and 90 kHz, which already can be guessed having a look at Fig. 19(c) and Fig. 19(d).

Thus, a band pass applied at this frequency results in the Fourier spectrum and filtered trace, cleaned of the high-frequent thereafter, shown in Fig. 20 and 21.
As expected, the high-frequent noise within both traces is filtered.

It has to be examined, whether the main peak is determined by the band pass between 10 - 90 kHz or a direct measurement of radio emission from lightning discharge. Therefore, a sharp delta distribution added to the trace is simulated by increasing the amplitude for two bins. This artificially prepared, the traces are Fourier transformed, then filtered and finally transformed. The results are shown in Fig. 22.

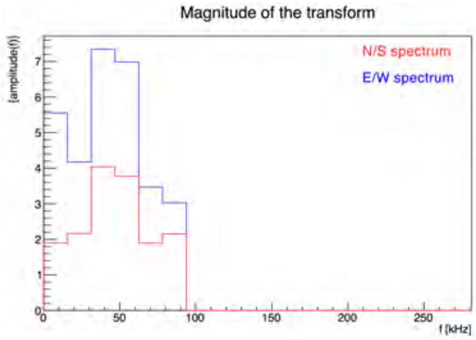

Figure 20: Zoomed N/S and E/W spectrum with high-cut at ≈ 90 kHz

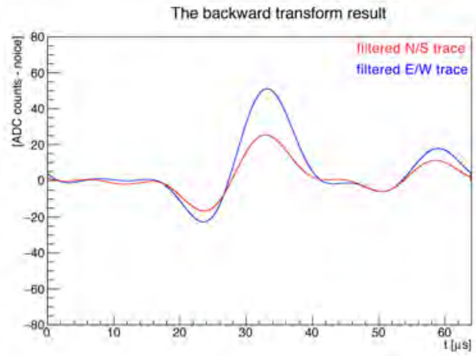

Figure 21: Filtered N/S and E/W trace

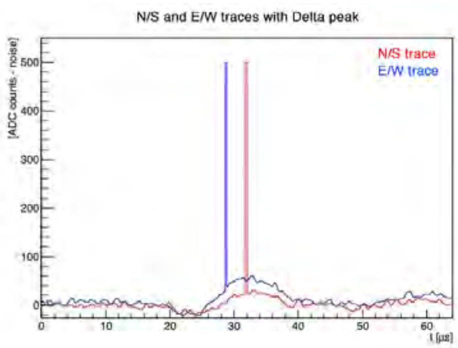

(a) Initial N/S and E/W radio trace with delta distributions

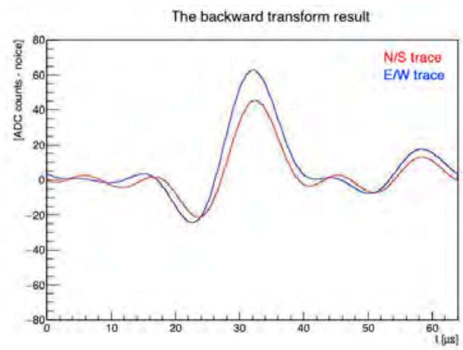

(b) Filtered N/S and E/W trace with delta distributions

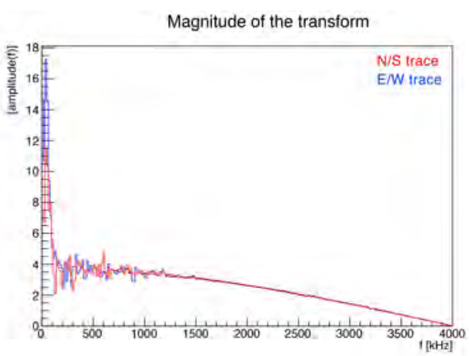

(c) Total spectrum for N/S and E/W with delta distributions

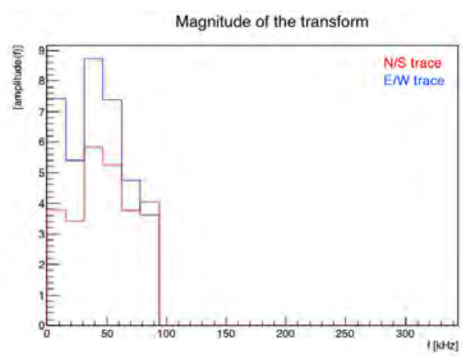

(d) Zoomed spectrum for N/S and E/W with delta distributions with high-cut at ≈ 90 kHz

Figure 22: Fourier transform with traces including an artificially added delta distribution

Comparing Fig. 21 and 22(b), it is observed that the antenna is not sensitive for fine time structures.

For the sake of clarity, the band-pass filtered and backward transformed traces of the N/S and E/W antenna with and without the delta distribution are shown separately in Fig. 23. The faint line represents the filtered trace without the delta distribution.

For each trace with a delta distribution only the amplitude varies slightly after applying a high cut on the frequency spectrum.

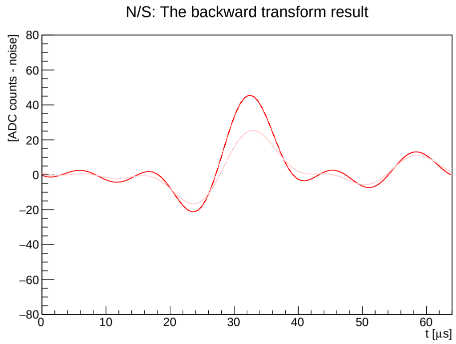

(a) Filtered N/S trace including delta distribution (faint line) and filtered N/S trace without delta distribution (normal line)

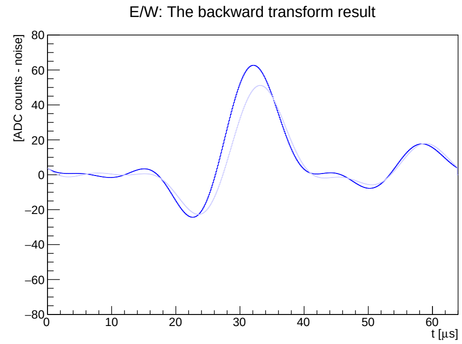

(b) Filtered E/W trace including delta distribution (faint line) and filtered E/W trace without delta distribution (normal line)

Figure 23: The difference of the cleaned N/S (left) and E/W (right) trace after the high-cut of 90 kHz

Consequently, the shape of the peak is a result of the band pass filter. This also means, that the StormTracker is not sensitive for frequencies beyond 90 kHz, which excludes unfortunately the measurement of the narrow bipolar pulses in the MHz region, described in Sec. 3.4.

The following analysis has to concentrate on other trace features.
In Sec. 5.2 the contents of the data files from CheckUp System were already mentioned. Thus, in the next section the polarity in the CheckUp files are compared to the traces of the lighting detector at the BUW.

6.4. StormTracker data comparison with CheckUp-System data

To exclude undesired noise pulses described in Sec. 5.2, the data from the three test detectors are compared to information available from CheckUp System. The result is a quality data set with real lightning events.

In the process of data analysis regarding data of the StormTrackers at the University of Wuppertal, almost no coincidences were found assuming a coincidence window of $\Delta t = 0$. To examine the distribution of differences, all time differences $t_1 - t_2$, $t_1 - t_3$, $t_2 - t_3$ for each detectors are filled in a histogram, see Fig. 25.

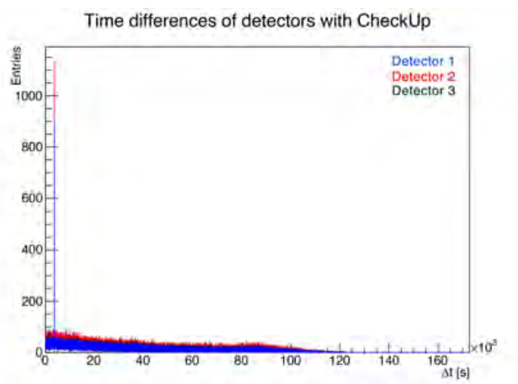

Figure 24: Histogram of time differences between the three detectors and Checkup

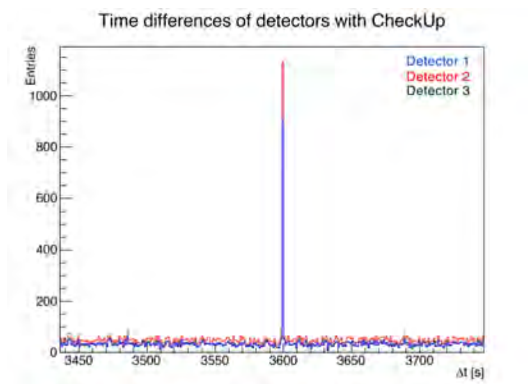

Figure 25: Zoomed histogram of time differences between the three detectors and Checkup

Obviously there is an offset of exactly one hour, most probably caused by UTC/CET offset, which is corrected for further analysis.

About 420 events were found in coincidence of all detectors at the test site and CheckUp and a coincidence window of $\Delta t = 3600$. This amount of events is used as a quality data set to compare the polarity entry in the CheckUp file with an estimation of the polarity extracted from the measured traces.
Fig. 26 shows a bar chart of the polarity categorization obtaining the values "positive" and "negative" in the CheckUp data.

In Sec. 3.2 it was mentioned, that about 90% are negative and 10% are positive charged cloud-to-ground lightning. In comparison of the quantities determined by CheckUp, these values show no agreement with lightning studies results.

The deviation could be explained by positive intracloud lightning within the CheckUp data, which is more common, but hard to detect because of the small amplitude of the dipole discharge and the pulse amplitude of the radio emission respectively [24], or the algorithm of CheckUp System simply does not identify the polarity correctly.

Figure 26: Bar chart of the polarity categorization obtaining the values "positive" and "negative" in the CheckUp data.

6.5. Analysis for polarity determination

In the final part of this thesis, possibilities are studied to extract the polarity feature of the east trace.

There is no information available from CheckUp from which measurement the polarity parameter is derived.
One guess is to examine solely the trace of the east/west antenna, as the determination of E_{thr} is performed on its basis, compare Sec. 6.1. Looking at the events using the EventBrowser and comparing it to the CheckUp information and the corresponding entry for the polarity shows a good agreement by first sight. In appendix A some examples are shown.

Because some traces (see Fig. 27) contain a huge amount of wiggles, subpeaks and ring buffer artifacts, an estimation of the polarity turned out to be difficult.

One solution to this problem is cutting off higher frequencies in the Fourier transform of each event in the quality data set of coincidences, so solely the main trace remains while sustaining enough information about the trace. As seen before, the antenna is only sensitive to frequencies below about 90 kHz, so features above that can be assumed to be disturbances caused by the electronics or picked up by cables.

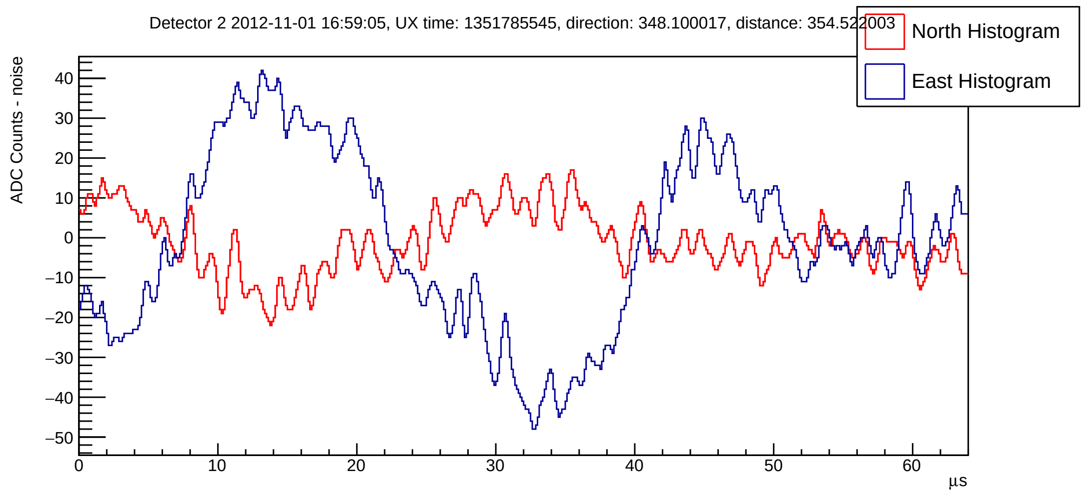

Figure 27: North/south, east/west trace with different sub peaks and ring buffer artifacts.

Having compared many peaks with the help of the EventBrowser developed within this thesis, a good guess for the duration of the assumed main peak is between

$$35\ \mu s \lesssim T_{\text{mainpeak}} \lesssim 45\ \mu\text{s}$$

resulting in a frequency of

$$22\ \text{kHz} \lesssim f_{\text{mainpeak}} \lesssim 28\ \text{kHz}$$

In the Fourier spectrum, one bin corresponds to $f \approx 15.6$ kHz, thus the backward Fourier transform is performed after canceling out frequencies above bin (4,3,2). This results in a high cut of $\approx f_{\text{highcut}}(62.4, 46.8, 31.2)$ [kHz] $= 0$. Fig. 28 demonstrates the influence of the different high cuts on the main peak for a lighting radio event.

While the Fourier transform works fine for the estimation of the sensitivity of the antenna, using the backwards transform traces for an estimation of the polarity yields the danger of filtering out important properties of the trace, as can bee seen in 28(d).

Instead of using the filtered traces, another strategy is pursued:
Because there are traces, which simply do not allow an estimation of the polarity (see Fig. 27), only traces which are relatively easy analyzed, are compared to the CheckUp file for each Detector 1, 2, 3 (in the following called D1, D2, D3.)

There are restrictions which are made in order to separate these traces. Fig. 29 illustrates possible restriction parameters.
The agreement with the CheckUp data is then plotted against the different restriction parameters, and the best fitting value can be estimated from having a look at the figures.

Firstly, only traces are compared which do not show a deviation of more than amplitudes A_{thresh} for D1, D2 and D3 as an absolute value in the first 150 bins of the buffersize ($\hat{=}$ 18.75 μs). This value guarantees that the first amplitude really is the main peak which triggered the detector and not an artifact of the ring buffer for events recorded after the triggered main peak or other sub peaks with small amplitudes. The artifact could consist

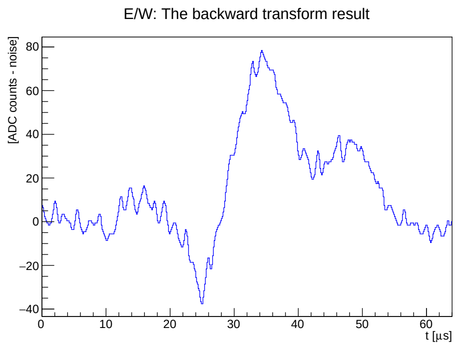

(a) Backwards transformed east/west trace with no high cut

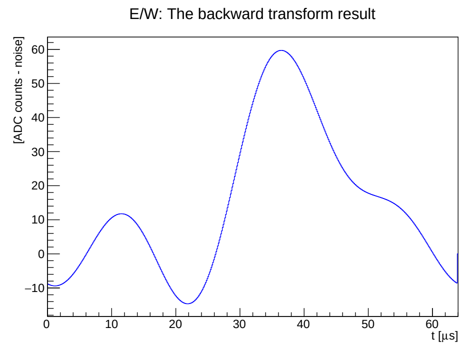

(b) Backwards transformed east/west trace with a high cut of 62.4 kHz

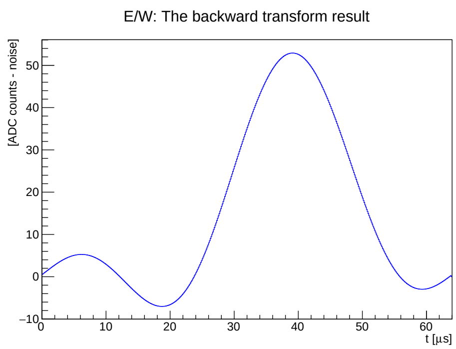

(c) Backwards transformed east/west trace with a high cut of 46.8 kHz

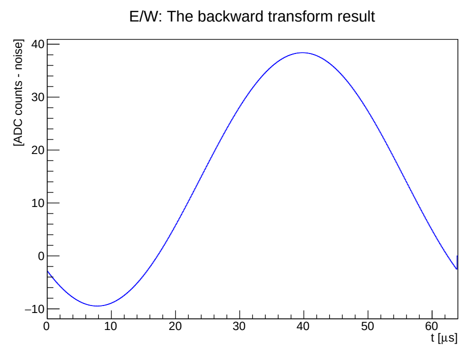

(d) Backwards transformed east/west trace with a high cut of 31.2 kHz

Figure 28: Fourier transform with traces including an artificially added delta distribution

of data stored after the triggered data for the actual event in the beginning of the trace.

The value of A_{thresh} is chosen by plotting the deviation against the acceptance of the CheckUp data for each detector, see Fig. 30, which is $A_{\text{thresh},1} \approx 17$, $A_{\text{thresh},2} \approx 29$ and $A_{\text{thresh},3} \approx 21$.

Secondly, the bin of the histogram's maximum of the trace bin_{max} is marked. At this point it is not known, whether the first main peak has a negative or positive polarity.
Then a first guess is made by having a look at the quantity of bins bins_{min} one has to subtract until a minimum appears, compare 29. A look at Fig. 31 allows a rough estimation of the values for D1, D2, D3 $\text{bins}_{\text{min},1} \approx 62 \mathrel{\hat{=}} 7.8\mu\text{s}$, $\text{bins}_{\text{min},2} \approx 65 \mathrel{\hat{=}} 8.1\mu\text{s}$ and $\text{bins}_{\text{min},3} \approx 62 \mathrel{\hat{=}} 7.8\mu\text{s}$.
From this value we can also estimate the average pulse length of $\overline{\text{T}} = 2 \cdot 7.9\mu\text{s} = 15.8\mu\text{s}$, assuming a sinusoid pulse, including the results from all three detectors.

If at the surrounding bins_{int} of this bin entry the count number is smaller than a assumed depth of minimum $Min = -35$, the maximum has a preceding minimum. Again, bins_{int} is plotted against the agreement to the CheckUp data and estimated to $\text{bins}_{\text{int},1} \approx 12$, $\text{bins}_{\text{int},2} \approx 12$ and $\text{bins}_{\text{int},3} \approx 13$, see Fig. 32.
It is then flagged as *negative* and compared to the coincidental event in the CheckUp data. If this is not the case, it is flagged as *positive* and again compared to the CheckUp data.

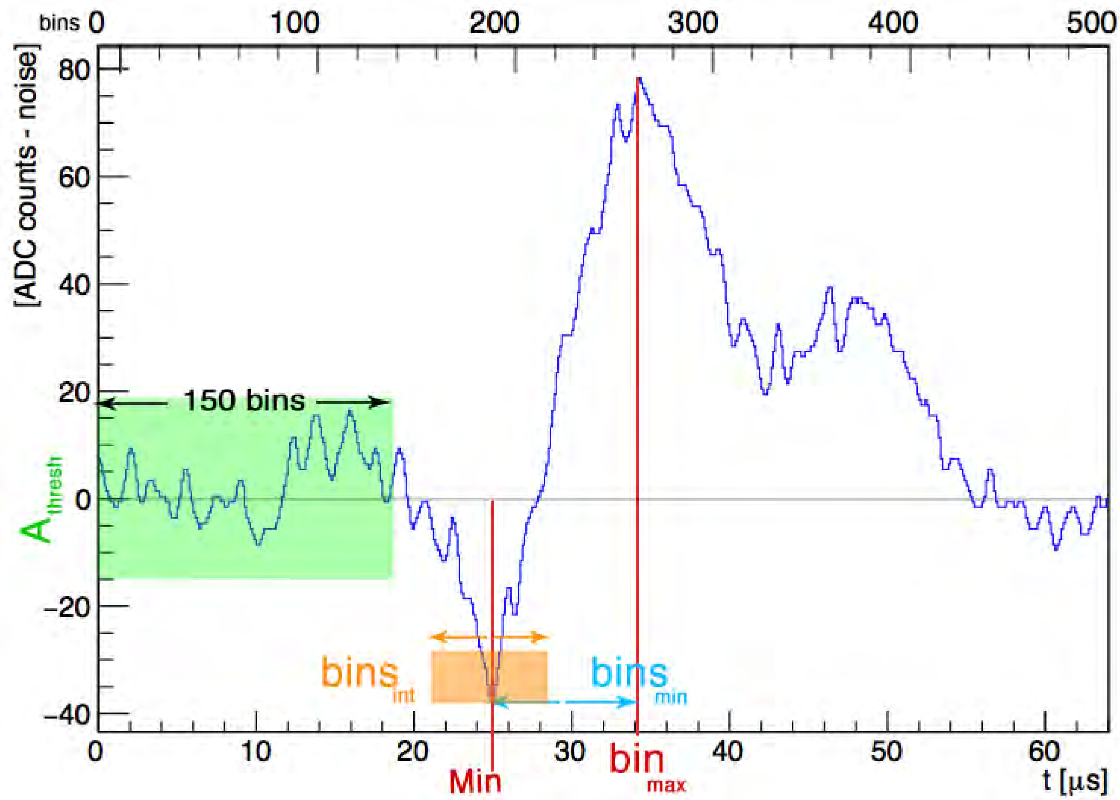

Figure 29: Illustration of restriction parameters

The overall number of agreements of coincidental events in all three detectors and the CheckUp time was 423.
After determination of the polarity on the basis of the presented mechanism and the tied down restriction parameters described above, from the 423 of the quality data sample matching events remain the following quantities: The initial events are for each detector the same. Applying the cut from the restriction parameters from D1 328, from D2 358 and from D3 363 events remain.

For D1 $\approx$ 37.7%, for D2 $\approx$ 48.9% and for D3 $\approx$ 45.2% are in agreement with the CheckUp data with respect to the polarity. These quota do not match the calculated polarity of traces from the three test site detectors in full agreement with the results from CheckUp.

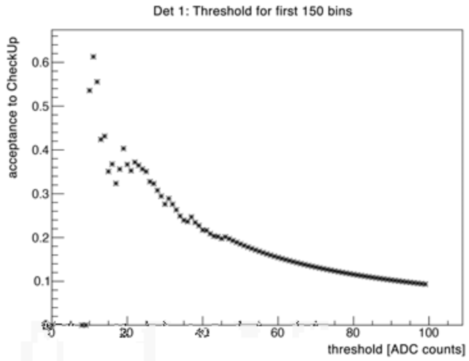

(a) $A_{thresh,1}$ for D1, estimated $A_{thresh,1} \approx 17$

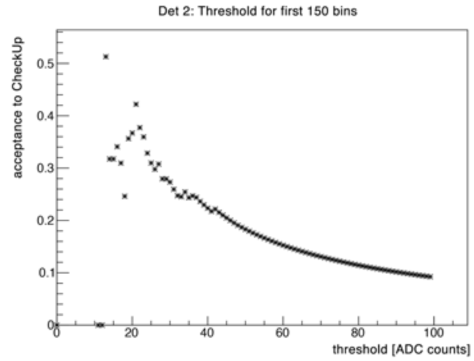

(b) $A_{thresh,2}$ for D2, estimated $A_{thresh,2} \approx 29$

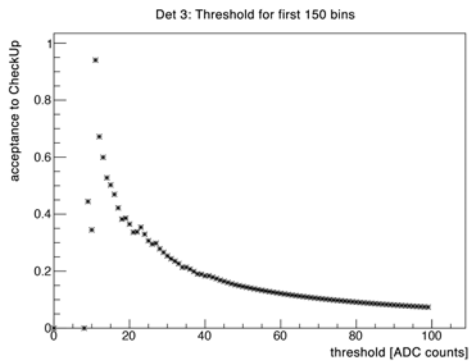

(c) $A_{thresh,3}$ for D3, estimated $A_{thresh,3} \approx 21$

Figure 30: Distributions for A_{thresh} contributing to agreement to CheckUp Data for D1, D2, D3.

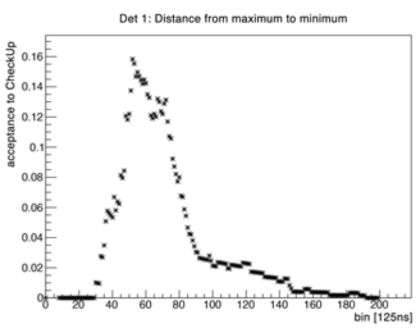

(a) $\text{bins}_{\text{min},1}$ for D1, estimated $\text{bins}_{\text{min}} \approx 62$

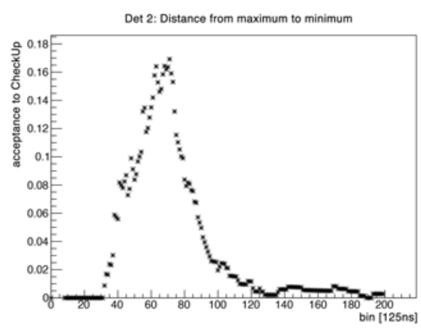

(b) $\text{bins}_{\text{min},2}$ for D2, estimated $\text{bins}_{\text{min}} \approx 65$

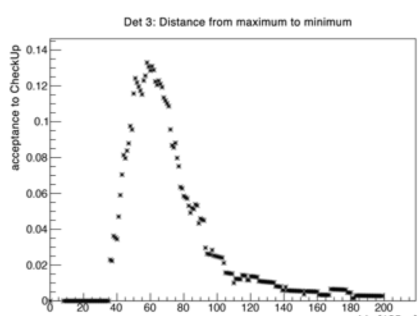

(c) bins_{min} for D3, estimated $\text{bins}_{\text{min}} \approx 62$

Figure 31: Distributions for bins_{min} contributing to agreement to CheckUp Data for D1, D2, D3.

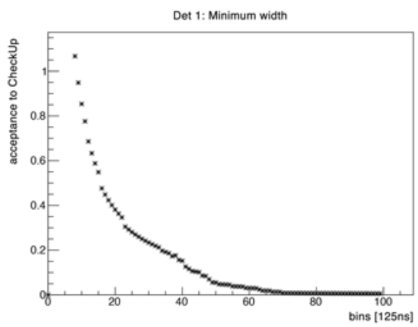

(a) $\text{bins}_{\text{int},1}$ for D1, estimated $\text{bins}_{\text{int},1} \approx 62$

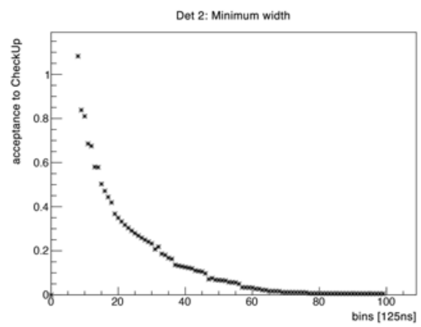

(b) $\text{bins}_{\text{int},2}$ for D2, estimated $\text{bins}_{\text{int},2} \approx 65$

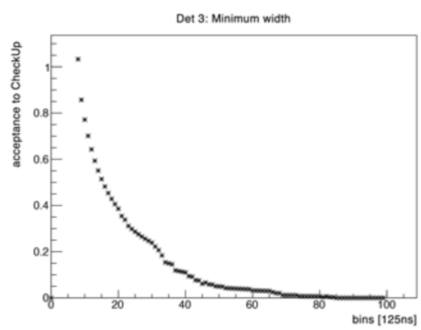

(c) $\text{bins}_{\text{int},3}$ for D3, estimated $\text{bins}_{\text{int},3} \approx 62$

Figure 32: Distributions for bins_{int} contributing to agreement to CheckUp Data for D1, D2, D3.

6.6. Brief analysis of multiplicity and pulse lengths

In this section, the results of a brief analysis of the trace features are presented. As already found out with the help of the EventBrowser in Fig. 17, there is a value $E_{\text{thr}} = [0; 1]$ set for each E/W antenna trace sample.
Having a look at Fig. 18, the value E_{thr} is set "1" for sequences of the trace, which moving average is above a certain value.
Under this assumption one can learn about the distribution of pulse lengths within the events and the amount of sequences, which hold a value $E_{\text{thr}} = 1$ for the time of the pulse length, which can be seen as the multiplicity, referring to the number of pulses within a trace.

For a dataset without restriction of the pulse length or the multiplicity of all detectors these distributions are shown in Fig. 33.

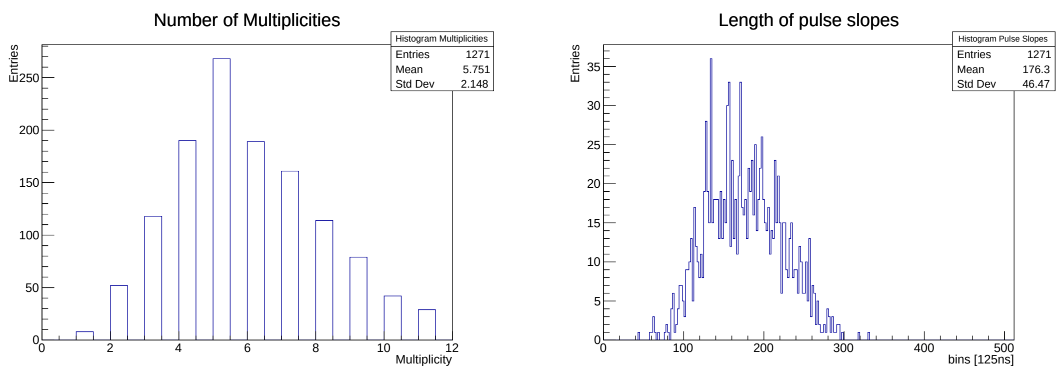

(a) Distribution of multiplicities within the trace for a dataset of lightning events without restriction of pulse length

(b) Distribution of pulse lengths for a dataset of lightning events without restriction of pulse length

Figure 33

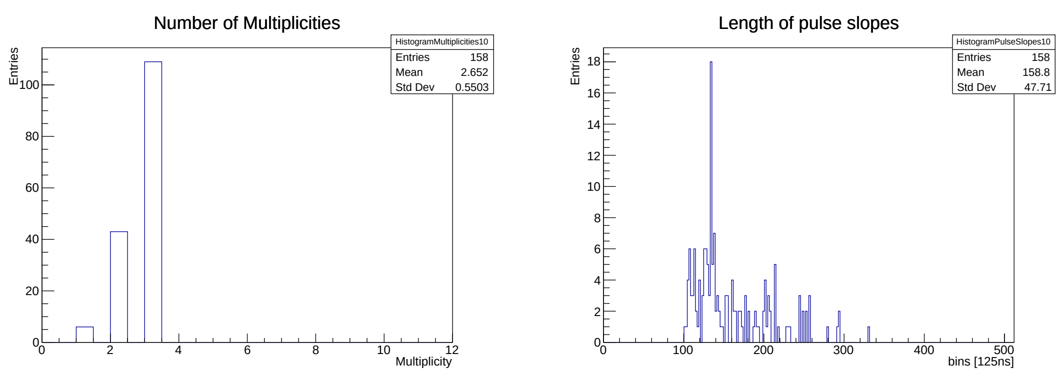

(a) Distribution of multiplicities within the trace for a dataset of lightning events without a minimum pulse length of 100 bins (or 12.5 μs)

(b) Distribution of pulse lengths for a dataset of lightning events with a minimum pulselength of 100 bins (or 12.5 μs)

Figure 34

The gross of the multiplicities is distributed in between four and five, with a pulse length of ≈150 bins (or 18.75 μs).

As can be seen for example in Fig. 18, at the end of the trace a very short sequence has $E_{\mathrm{thr}} = 1$ set. To cut off these short pulses a restriction is made for the pulse length to be larger than 100 bins (or 12.5 μs) and a cut on the number of multiplicities higher than three. The result is shown in Fig. 34.

The result is as expected. In Fig. 34(a) the cut off applies for a number of multiplicities higher than three and leads to a better definition of smaller pulse lengths, compare Fig. 34(b).

7. Conclusion

In this thesis we investigated the traces of the StormTrackers which are deployed at the Pierre Auger Observatory.
To have a comfortable tool and to get an intuitive impression for the available data, the first step was to develop a root GUI, the EventBrowser, which generates a list of the selected detectors' coincidental events and plots the associated N/S and E/W traces including all information about the event. It was made available in a svn repository at http://at-web.physik.uni-wuppertal.de/svn/LightningViewer.

In order to learn, whether the frequency spectrum of the waveforms results from the lightning or from the antennas band-pass, a Fourier transform was performed with a simulated high-cut at the expected frequency range of the antenna and an artificially created delta distribution.
The result was, that the antenna is capable of measuring radio pulse within the range of about $15.6 - 90$ kHz.
Unfortunately, this limits the possibility of measuring features of the narrow bipolar pulses in the MHz region, which are created during EAS and intracloud lightning.

It was found, that only the E/W trace of the antenna contributes to the determination of polarity and that an electrical field value is saved according to a sudden change of the slope of the east trace.

The relation abundance of positive and negative flagged events in the CheckUp data in Fig. 26 deviates from the expected lightning statistics and appears suspicious. It is not known, in which way CheckUp System determines the polarity. An algorithm has been developed within this thesis in Sec. 6.5. The agreement with the CheckUp estimation has been found for the detectors to be for D1 $\approx$ 37.7%, for D2 $\approx$ 48.9% and for D3 $\approx$ 45.2%. Therefore no significant connection between the calculated polarity of traces from the three test site detectors and the results from CheckUp was found.
The main reason for the bad agreement lies in the quality of the traces, which in many cases make a proper analysis within the timeframe of this thesis impossible, see Fig. 27 . But is also has to be considered, that the CheckUp predicted polarity does not agree with the 90% negative and 10% positive polarity. In this case, the bad agreement makes sense. There is also the possibility, that the polarity of the pulses do not correlate to the sign of the discharge and the quality of the CheckUp information might be low, giving rise to the poor correlation with the measurements derived here.
Sec. 6.6 presented a brief overview of the multiplicity of a dataset of lightning events and an average pulse length.
Despite of limited possibilities of extracting information about the lightning itself, the Boltek StormTracker, deployed as a lightning detector station serves well for the trigger of a lightning flag for the more precise facilities like AREA at the Pierre Auger Observatory, making lightning and cosmic ray correlation studies possible by measuring the mentioned narrow bipolar pulses during lighting and EAS in the VHF radio band.

A. Comparison of the polarity from traces to Checkup file

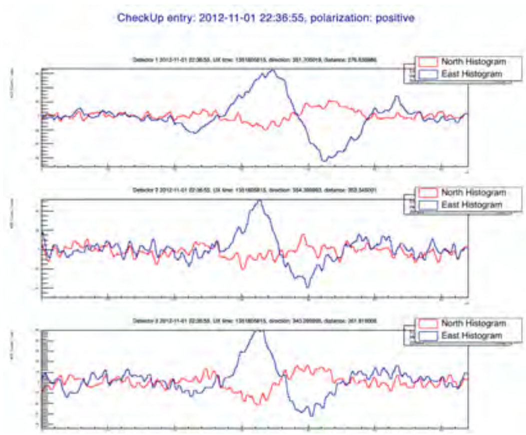

(a) CheckUp entry: 2012-11-01 22:36:55, polarity: positive

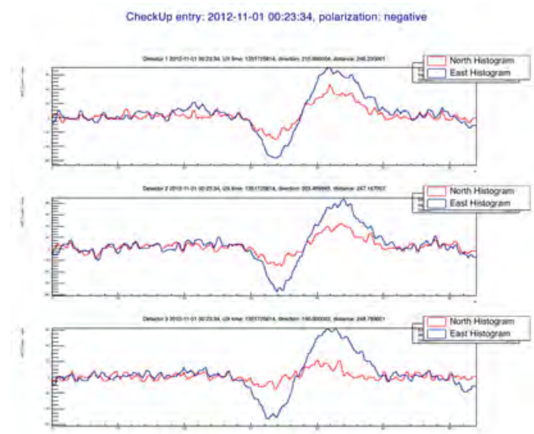

(b) CheckUp entry: 2012-11-01 00:23:34, polarity: negative

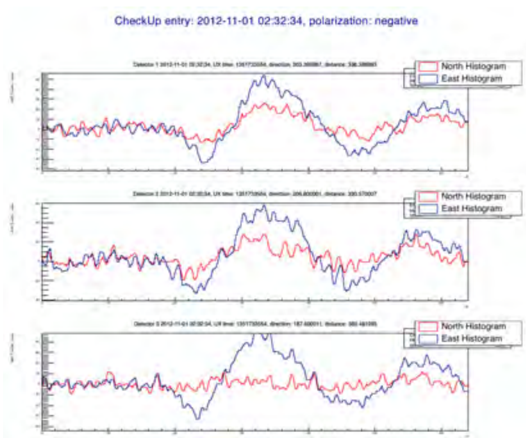

(c) CheckUp entry: 2012-11-01 02:32:34, polarity: negative

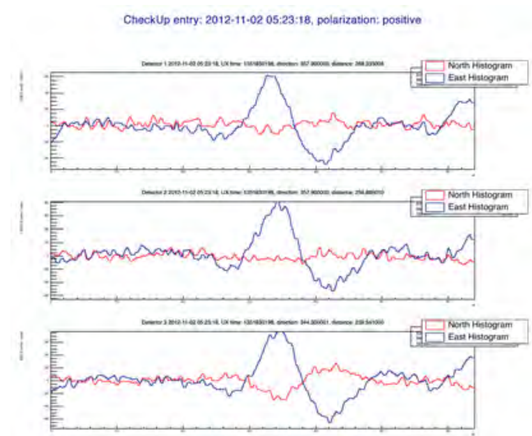

(d) CheckUp entry: 2012-11-02 05:23:18, polarity: positive

Figure 35: Four examples of lightning detector events with obvious polarity in the EventBrowser and CheckUp source file's polarity entry in good agreement.

References

[1] A.V. Gurevich. L.M. Duncan, Karashtin, K.P. Zybin, *Radio emission of lightning initiation*, Physics Letters A 312 (2008)

[2] Cosmic Rays, https://en.wikipedia.org/wiki/Cosmic_ray (retrieved on 03.04.2016)

[3] K.H. Kampert, *Vorlesung Einfuehrung in die Astroteilchenphysik* (2004)

[4] Diego Casadei, *Direct measurement of galactic cosmic ray fluxes with the orbital detector AMS-02* (2003)

[5] News from Space Radiation Lab at CIT, http://www.srl.caltech.edu/ACE/ACENews/ACENews83.html (retrieved on 22.03.2016).

[6] Antarctic Glaciers, http://antarcticglaciers.org (retrieved on 31.03.2016)

[7] Alexander V. Gurevich and Kirill P. Zybin, *Runaway Breakdown and the Mysteries of Lightning*, Physics Today (2005)

[8] Joseph R. Dwyer, Martin A. Uman, *The Physics of Lightning*, Physics Reports (2014)

[9] H. A. Bethe, L.C. Maximon *Theory of Bremsstrahlung and Pair Production. I. Differential Cross Section* (1953)

[10] T. C. Marshall, M. D. McCarthy, W. D. Rust, J. Geophys. Res. 100, 7097 (1995). T. C. Marshall et al., Geophys. Res. Lett. 32, L03813 (2005).

[11] A. V. Gurevich, K. P. Zybin, Phys. Usp. 44, 1119 (2001)

[12] W.D. Apel et al. *Thunderstorm Observations by Air-Shower Radio Antenna Arrays* (2013)

[13] David M. Le Vine *Review of Measurements of the RF Spectrum of Radiation from Lightning*, NASA Technical Memorandum 87788 (1986).

[14] M. Le Boulch, J. Hamelin, and C. Weidman. *Uhf-vhf radiation from lightning*. Electromagnetics, 287,Äì331 (1987).

[15] A. V. Gurevich, L. M. Duncan, A. N. Karashtin, K. P. Zybin, Phys. Lett. A 312, 228 (2003).

[16] The Pierre Auger Colloboration, *The Pierre Auger Cosmic Ray Observatory* (2015)

[17] Pierre Auger Observatory, https://en.wikipedia.org/wiki/Pierre_Auger_Observatory (retrieved on 03.04.2016)

[18] The Pierre Auger Collaboration *Probing the radio emission from air showers with polarization measurements* (2014)

[19] The Pierre Auger Collaboration *The Pierre Auger Observatory V: Enhancements* (2011)

[20] The Pierre Auger Collaboration *HEAT - a low energy enhancement of the Pierre Auger Observatory* (2011)

[21] The Pierre Auger Collaboration, *Radio detection of high-energy cosmic rays with the Auger Engineering Radio Array* (2015)

[22] Lukas Niemietz, PhD thesis, *Lightning Detection at the Pierre Auger Observatory* (2016)

[23] Boltek Corperation *StormTracker Lightning Detector (with PCI style receiver card) - Installation/Operators Guide* (2014)

[24] Aninoquisi Software Design *Lightning/2000 User's Manual* (2016)

List of Figures

1 Cosmic Ray Flux with respect to the energy, showing three main regions, from [2] 4
2 Hillas Plot showing magnetic field of possible sources with respect to the size, from [3] 4
3 Schematic representation of an extensive air shower from cosmic rays, from [6] 6
4 Relative abundances with respect to the atomic number Z from cosmic rays in comparison to the solar system , from [5] 6
5 Scheme of different kind of lightnings: Intracloud, inter cloud, cloud-to-ground and charge regions within clouds, from [8]. 8
6 Schematic representation of the negative cloud-to-ground lightning discharge process, from [8]. 9
7 Results of measurements [10] of the electric field including zones of lowered threshold due to runaway breakdown with respect to the atmospheric height, from [7]. 10
8 Braking force F/F_{min} with respect to the electron energy in MeV: Runaway region for $\epsilon > \epsilon_c$, from [7]. 10
9 Radio emission spectrum from lightning, determined from a distance of 10 km, from [14]. 12
10 Theoretical predictions for radio pulse forms, modified from [7]. 12
11 Map of the Pierre Auger Observatory, each black dot represents a SD tank. The whole area is surrounded by four FD sites, each equipped with 6 telescopes, from [17]. 13
12 SD tank with labels of main components, from [16]. 13
13 Summary of atmospheric conditions variables, from [16] 15
14 Locations of atmospheric monitoring devices, modified from [16] 15
15 Boltek StormTracker: PCI card with ethernet-connected antenna 16
16 Monitoring of lightning events at the PAO, retrieved on 07.04.2016. 18
17 Snapshot of the EventBrowser for a randomly selected event with one (top), two (middle) and there (bottom) coincident stations. The list on the left side contains, depending on the selection of the three detectors, the intersection of coincident events and can be drawn to the right canvas. 20
18 Example N/S and E/W trace for a defined lighting event with marked E_{thr} value, yellow for $E_{\text{thr}} = 1$, blue for $E_{\text{thr}} = 0$ 21
19 Initial traces for east/west and north/south orientation 22
20 Zoomed N/S and E/W spectrum with high-cut at ≈ 90 kHz 23
21 Filtered N/S and E/W trace 23
22 Fourier transform with traces including an artificially added delta distribution 23
23 The difference of the cleaned N/S (left) and E/W (right) trace after the high-cut of 90 kHz 24
24 Histogram of time differences between the three detectors and Checkup . . . 25
25 Zoomed histogram of time differences between the three detectors and Checkup 25
26 Bar chart of the polarity categorization obtaining the values "positive" and "negative" in the CheckUp data. 26
27 North/south, east/west trace with different sub peaks and ring buffer artifacts. 27
28 Fourier transform with traces including an artificially added delta distribution 28
29 Illustration of restriction parameters 29
30 Distributions for A_{thresh} contributing to agreement to CheckUp Data for D1, D2, D3. 30

31 Distributions for bins_{min} contributing to agreement to CheckUp Data for D1, D2, D3. 30
32 Distributions for bins_{int} contributing to agreement to CheckUp Data for D1, D2, D3. 31
33 32
34 32
35 Four examples of lightning detector events with obvious polarity in the EventBrowser and CheckUp source file's polarity entry in good agreement. . . 35

Eidesstattliche Erklärung

Hiermit versichere ich, die vorliegende Arbeit selbstständig und unter ausschließlicher Verwendung der angegebenen Literatur und Hilfsmittel erstellt zu haben.

Die Arbeit wurde bisher in gleicher oder ähnlicher Form keiner anderen Prüfungsbehörde vorgelegt und auch nicht veröffentlicht.

Ich versichere, dass die eingereichte schriftliche Fassung der auf dem beigefügten Medium gespeicherten Fassung entspricht.

Wuppertal, den

(Simon Strotmann)